Research

Author for correspondence:
L. Mahadevan
e-mail: lmahadev@g.harvard.edu

THE ROYAL SOCIETY
PUBLISHING

Beak morphometry and morphogenesis across avian radiations

Salem Mosleh[1,†], Gary P. T. Choi[4,†], Grace M. Musser[5,6], Helen F. James[6], Arhat Abzhanov[7,8] and L. Mahadevan[1,2,3]

[1]John A. Paulson School of Engineering and Applied Sciences, [2]Department of Organismic and Evolutionary Biology, and [3]Department of Physics, Harvard University, Cambridge, MA 02138, USA
[4]Department of Mathematics, The Chinese University of Hong Kong, Hong Kong, Hong Kong
[5]Department of Integrative Biology, University of Texas at Austin, Austin, TX 78712, USA
[6]Department of Vertebrate Zoology, National Museum of Natural History, Smithsonian Institution, Washington, DC 20560, USA
[7]Department of Life Sciences, Imperial College London, Ascot SL5 7PY, UK
[8]Natural History Museum, Cromwell Road, London SW7 5BD, UK

SM, 0000-0002-6988-2991; GPTC, 0000-0001-5407-9111; AA, 0000-0002-8577-8318; LM, 0000-0002-5114-0519

Adaptive avian radiations associated with the diversification of bird beaks into a multitude of forms enabling different functions are exemplified by Darwin's finches and Hawaiian honeycreepers. To elucidate the nature of these radiations, we quantified beak shape and skull shape using a variety of geometric measures that allowed us to collapse the variability of beak shape into a minimal set of geometric parameters. Furthermore, we find that just two measures of beak shape—the ratio of the width to length and the normalized sharpening rate (increase in the transverse beak curvature near the tip relative to that at the base of the beak)—are strongly correlated with diet. Finally, by considering how transverse sections to the beak centreline evolve with distance from the tip, we show that a simple geometry-driven growth law termed 'modified mean curvature flow' captures the beak shapes of Darwin's finches and Hawaiian honeycreepers. A surprising consequence of the simple growth law is that beak shapes that are not allowed based on the developmental programme of the beak are also not observed in nature, suggesting a link between evolutionary morphology and development in terms of growth-driven developmental constraints.

1. Introduction

Avian adaptive radiations, such as those associated with Darwin's finches and Hawaiian honeycreepers (figure 1*a*), provide concrete examples of how a species can diversify, with the beak evolving into a variety of forms that enabled different specialized functions. To elucidate this diversification of form, we need to quantify both the nature and the extent of variation in beak shapes and how this variation enables function (e.g. feeding and vocalization). In addition, since this variation in shape is generated by modifications of a developmental programme to produce new forms, it is equally important to describe these three aspects of beak shape evolution (form, function and development) within a common framework that can further illuminate the evolvability of adaptive radiation. Here, using micro-computed tomography (μCT) scans of Darwin's finches, Hawaiian honeycreepers and their relatives, we quantify beak and skull shape variation, and link it to their evolution and development.

Beak shapes have been quantified using discrete measurements, such as length, width and depth, or using a set of landmarks—identifiable points that are common to all studied specimens [3,4]. While these methods are valuable in characterizing beak shape variation [5–7], they do not explicitly capture the rich geometry of beak shape parametrized by the curvature of its surface, unless sliding semilandmarks are used [8,9]. To overcome the challenges associated with
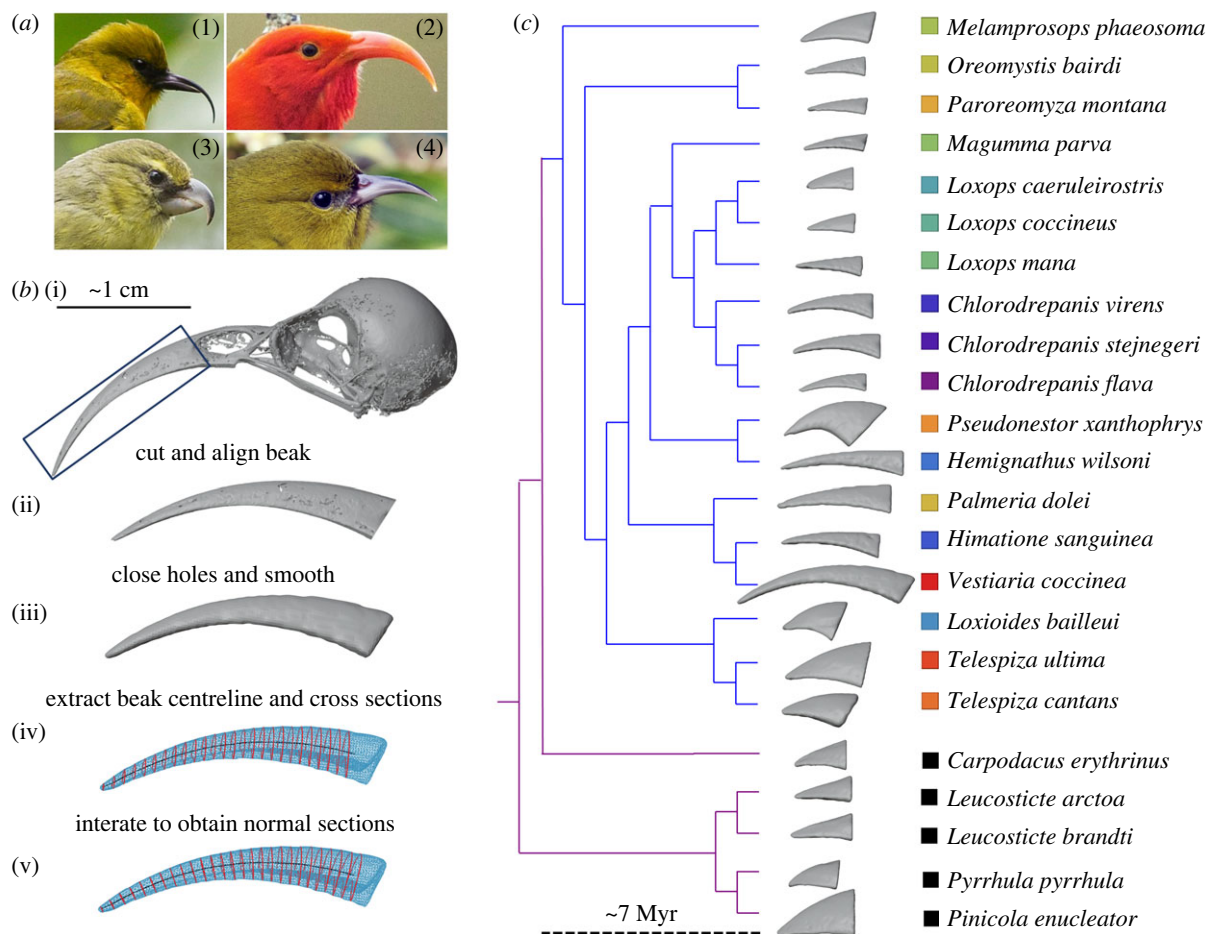
Figure 1. Beak morphology and phylogeny of Hawaiian honeycreepers. (*a*) Examples showing the diversity of beak shapes observed for Hawaiian honeycreepers: (1) *H. wilsoni*, (2) *V. coccinea*, (3) *P. xanthophrys* and (4) *C. flava*. (*b*) Steps used in our analysis to extract beak shapes, centrelines and cross sections (see electronic supplementary material for details). (i) The skull is aligned so that its long axis is in the *x*-direction. (ii) The beak is cut from the skull using the most basal plane normal the *x*-axis that does not include the nares (nostrils), then rotated so that its major axis is along the *x*-direction, and (iii) smoothed to remove holes from the mesh. (iv) starting with vertical cross sections perpendicular to the *x*-axis, we find a test centreline as the centre of mass (assuming uniform density) for each cross section. New cross sections are obtained normal to the generated centreline. Iterating this procedure, we get the final centreline and cross sections shown in (v). (*c*) The phylogeny of honeycreepers and their relatives based on [1]. Taxonomic nomenclature follows [2], except that the genus *Vestiaria* is not merged with *Drepanis*.

landmark-based morphometrics [10], landmark-free methods that avoid the need to manually select a set of landmarks on a structure have been developed, for example, using smooth transformations [11] or Fourier transforms [12]. Complementing these morphometric approaches, researchers have also suggested generative models for the morphogenesis of shapes modelled geometrically, with each specimen represented by the values of the best-fit model parameters [13–15]. This leads to theoretical morphospaces and allows for investigating why some forms exist in nature and others do not, either due to functional or ontogenetic constraints [13].

Here, we take both these approaches, drawing on and generalizing our recent work on the finch beak [16], to quantify the range of avian beak shapes and provide a biophysical model for their morphogenesis. We first describe the upper surface of the beak using three complementary landmark-free approaches. In the first approach, the beak shape is represented as a surface with curvature linearly decreasing with distance from the tip [16]. To accommodate the highly curved honeycreeper beaks and motivated by beak ontogeny, we then extract the upper bill centreline, along with its normal cross sections as a function of distance from the tip to further elucidate the geometry of beak shape variation. Lastly, we use an independent approach, based on the

Hausdorff distance, to validate results on the distribution of species within each phylogenetic group in morphospace. This third approach is flexible enough to apply equally to beaks and skulls without introducing landmarks or parametric equations. While all our morphometric approaches give similar qualitative conclusions regarding the distributions of beaks and skulls in morphospace, consistent with prior results using landmark morphometrics [7], we discover further geometric regularities in beak shapes and computationally link morphology to development and function.

Next, motivated by studies of beak growth during embryonic development [17,18] that show that a group of proliferating cells near the tip of the developing beak form a growth zone that defines the shape of the beak as it shrinks over time, we investigate how transverse beak cross sections normal to the centreline change as they approach the tip of the beak. We observed that beak cross sections change shape over time, becoming more convex and circle-like the closer they are to the tip, contrary to the previous assumption that the growth zone will shrink uniformly (without change in shape) over time [18]. This observation motivates us to use a variant of the modified mean-curvature flow model of growth zone evolution [16] by allowing a highly curved region near its boundary to shrink (stop dividing) at a higher rate compared with cells in
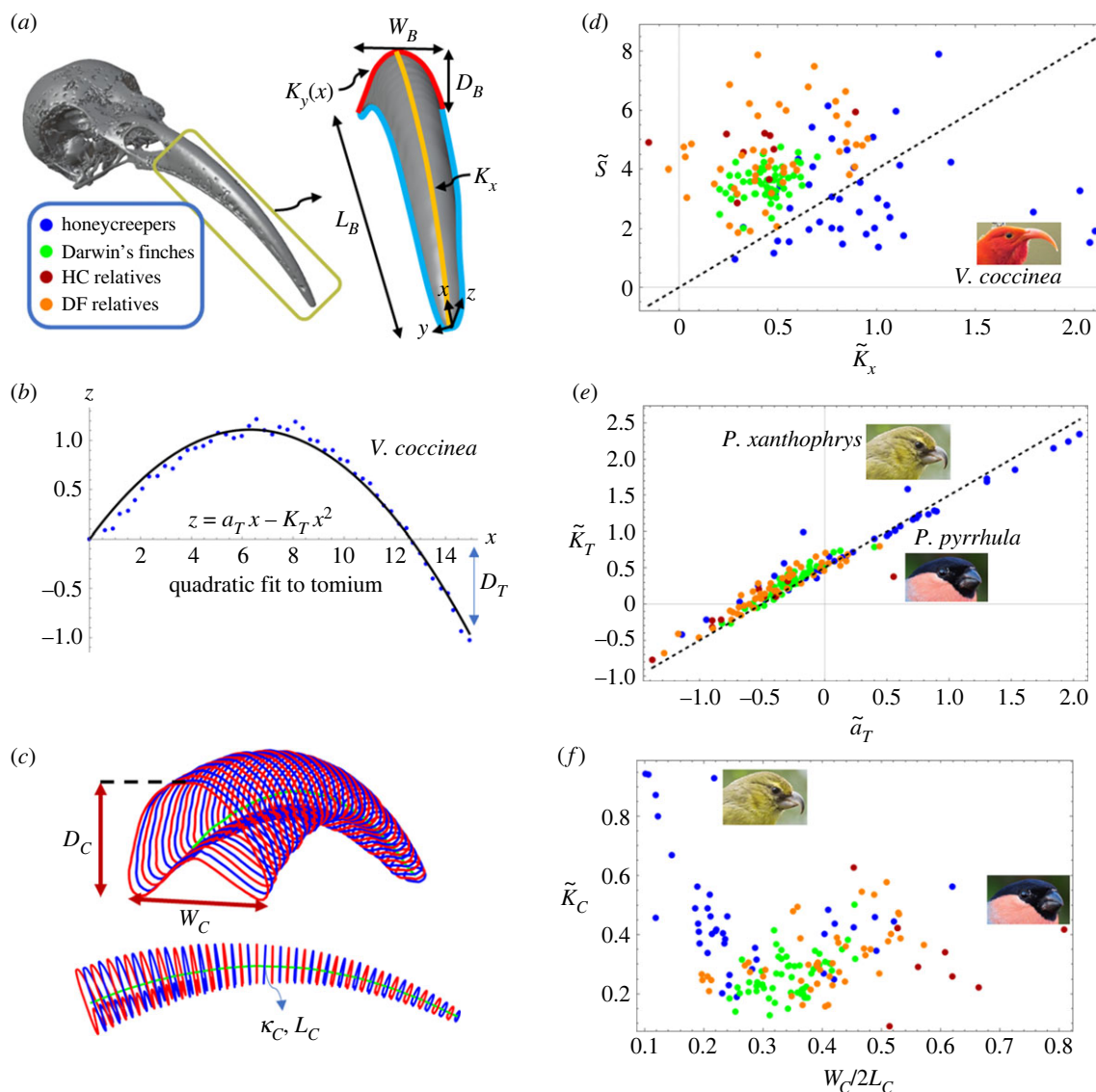
Figure 2. Evolutionary morphospace of beaks. (a) The extracted upper beak (right) from a *V. coccinea* skull (left). The beak axes are aligned with its principal directions (figure 1b). The functional form $z = (D_B + \kappa_x L_B^2)(x/L_B) - \kappa_x x^2$ approximates the midsagittal curve ($y = 0$) shown in yellow. Transverse sections (red) also have parabolic form with curvatures varying with distance from the tip according to $\kappa_y(x) = \kappa_{tip} - S\,x$. The tip curvature, κ_{tip}, is extrapolated from the relation $\kappa_{tip} \equiv \kappa_y(0)$. (b) The extracted tomium of the beak projected onto the xz−plane and the corresponding parabolic fit. (c) The morphological variables defined by the beak centreline, where L_C is its length and κ_C is its curvature. At the base of the beak, the cross section is characterized by its depth D_C and width W_C. (d) Beak morphospace defined by the variables $\tilde{\kappa}_x = L_B^2 \kappa_x / D_B$ and $\tilde{S} = L_B W_B^2 S / D_B$ for 151 specimens from four groups, colour coded as shown in (a). (e) The morphospace defined by the dimensionless tomium parameters $\tilde{a}_T = L_B a_T / D_B$ and $\tilde{\kappa}_T = L_B^2 \kappa_T / D_B$. The fact that most points are close to the dashed curve, defined by $\tilde{\kappa}_T = 0.5 + \tilde{a}_T$, indicates that $D_T \approx 0.5\,D_B$ for almost all beaks in our dataset as explained in the text. (f) Beak morphospace defined by the aspect ratio $W_C/(2 L_C)$ and dimensionless centreline curvature $\tilde{\kappa}_C \equiv \kappa_C L_C$.

the bulk of the growth zone. This tissue scale behaviour can emerge from a morphogen diffusion and degradation, where cells continue dividing if the concentration of this morphogen is above a threshold value [16]. By additionally allowing changes in the growth direction that can generate beaks with highly curved centrelines, we show that we can generate the observed beak shapes of both Darwin's finches and Hawaiian honeycreepers.

2. Evolutionary morphospace of beaks

(a) Constructing morphospaces

In figure 1b,c, we show beak meshes from honeycreepers ($n = 41$) and their relatives ($n = 9$) along with their phylogenetic

relationships (see electronic supplementary material, figure S1 for views of the entire skull). Our dataset, with 151 total specimens, also includes Darwin's finches ($n = 54$) and their relatives ($n = 47$). To quantify their three-dimensional shapes, we extract and smooth the three-dimensional surfaces of the bones of upper beaks from μCT-scans of the skulls and, for each smoothed beak mesh, automatically extract its centreline and beak cross sections normal to it (see figure 1; electronic supplementary material, figure S2 for details of smoothing and centreline extraction).

To extract the upper surface of the beak, we first find the tomium (cutting edge of the beak) as the points with minimum and maximum lateral coordinates (y-axis in figure 2a). The tomium then separates the upper and lower surfaces of the beak, which we orient so that the origin of the coordinate

system is at the tip of the upper surface, with axes oriented to correspond to the principal axes (electronic supplementary material, figure S3). We find that the following paraboloidal profile, which was introduced as a fit to the beaks of Darwin's finches in [16], captures the upper surface of the beak for the samples in our dataset (electronic supplementary material, figure S4):

$$z_U(x, y) = a_U x - \kappa_x x^2 - (\kappa_{tip} - S x) y^2, \tag{2.1}$$

where the subscript U denotes the upper surface, a_U gives the slope of the midsagittal section ($y = 0$) near the tip, κ_x is the curvature of the midsagittal section, κ_{tip} is the curvature in the transverse direction at the tip and S represents the 'sharpening rate' of the beak curvature towards the tip. Since the size of the cross section shrinks to zero at the tip, the parameter κ_{tip} is extracted from the linear fit of the transverse curvature $\kappa_y \equiv \kappa_{tip} - S x$. The beak is also characterized by its length L_B, width W_B, and depth D_B, where the subscript B denotes measurements aligned with the bounding box of the beak oriented along the principal directions (figure 2a). To compare beak shape across species, we remove the effect of scale and consider the dimensionless shape variables

$$\tilde{a}_U = \frac{L_B}{D_B} a_U, \quad \tilde{\kappa}_x \equiv \frac{L_B^2}{D_B} \kappa_x, \quad \tilde{\kappa}_{tip} \equiv \frac{W_B^2}{D_B} \kappa_{tip} \text{ and } \tilde{S} \equiv \frac{L_B W_B^2}{D_B} S. \tag{2.2}$$

To describe the shape of the tomium, we project the extracted tomium points onto the xz-axis and fit the resulting curve to a parabola,

$$z_T(x, y) = a_T x - \kappa_T x^2, \tag{2.3}$$

which gives a good fit as shown in figure 2b. The three-dimensional tomium curve can then be found as the intersection of the upper beak surface given by equation (2.1) and the surface given by equation (2.3). We also define normalized tomium parameters as $\tilde{a}_T \equiv L_B a_T / D_B$ and $\tilde{\kappa}_T \equiv L_B^2 \kappa_T / D_B$. Knowing the upper beak surface and tomium, equations (2.1)–(2.3), we can define the beak depth and width as a function of the coordinate x. The depth is defined as $D(x) \equiv z_U(x, 0) - z_T(x, 0)$, while the width is defined through the equation $z_U(x, W(x)/2) = z_T(x, W(x)/2)$, which leads to

$$W(x) = \sqrt{\frac{4D(x)}{\kappa_{tip} - Sx}} = \sqrt{\frac{4(a_U - a_T)x - 4(\kappa_x - \kappa_T)x^2}{\kappa_{tip} - Sx}}. \tag{2.4}$$

Comparisons of this equation with data are given in electronic supplementary material, figure S3.

To elucidate the role of centreline curvature in honeycreeper beak shape variation, we compute the arc-curvature of the beak centreline, κ_C, by fitting the centreline to a circular arc (figure 2c; electronic supplementary material, figure S3). A circular arc is used in this case, since the obtained curvature will not depend on the overall rotation of the beak—unlike a parabolic fit, which changes depending on the choice of the x and y axes. In addition, as shown in figure 2c, we define centreline adapted length, width and depth (L_C, W_C, D_C) and corresponding centreline adapted coordinates (x_C, y_C, z_C), where x_C is the arc-length coordinate along the beak centreline and (y_C, z_C) represent the remaining two orthogonal directions. We also define a dimensionless curvature $\tilde{\kappa}_C = L_C \kappa_C$ and aspect ratio W_C / L_C between the width of the beak's basal cross section and the centreline length.

To elucidate the statistical distribution of beaks in morphospace, and the covariation between beak and skull shapes, we performed a surface-based morphometric analysis for the beaks and skulls in our dataset. We first normalized each surface mesh based on the distance between the beak tip and the centroid of the mesh. Then, for each pair of specimens, we searched for an optimal rigid transformation (i.e. a combination of translations and rotations) to align them and computed the symmetric Hausdorff distance between them [19,20]. The advantage of using this metric is that it does not depend on a correspondence between points on the meshes that may have different numbers of points—it is computed by first finding for each vertex on one mesh the minimum distance to the other mesh, and then taking the maximum value across all these pointwise distances. Once we obtained the Hausdorff distance measure for all pairs of specimens, we used multidimensional scaling (MDS) to represent all specimens on the two-dimensional plane (figure 3), where distance between points in this plane are as close as possible to the computed Hausdorff distance between each pair of meshes [21,22]. Repeating this for beaks and skulls separately, results in coordinates that describe the beak and skull shapes. In addition, by using affine (rigid, scaling and shear) transformations to optimally align meshes we obtained MDS coordinates that indicate how well two shapes can be transformed into each other with this set of transformations [23].

(b) Patterns in morphospace

The dimensionless parameters that we use to characterize beak size and shape given in equation (2.2) are not all independent. Indeed, using equation (2.1) and the relation $D_B = z_U(L_B, 0)$, we obtain $\tilde{a}_U = 1 + \tilde{\kappa}_x$. In addition, since the curvature of the parabola at the base of the beak is given as $\kappa_y(L_B) = 4W_B^2/D_B$, we have the identity $\tilde{\kappa}_{tip} = 4 + \tilde{S}$, which we verify by calculating the Pearson correlation coefficient between the two quantities across our 151 samples ($Cor[\tilde{S}, \tilde{\kappa}_{tip}] \approx 0.97$) and noting that specimens are close to the plane $\tilde{\kappa}_{tip} = 4 + \tilde{S}$ in morphospace (electronic supplementary material, figure S5A). This reduces the morphospace of beak shapes to an overall size (which may be taken as the length L_B), two aspect ratios associated with the relative depth D_B/L_B and width W_B/L_B and two scaled curvature parameters $\tilde{\kappa}_x$, $\tilde{S}$.

By looking at the samples in the morphospace ($\tilde{\kappa}_x$, $\tilde{S}$) (figure 2d), we note that the region $4\tilde{\kappa}_x > \tilde{S}$ is only occupied by honeycreepers. The constraint $4\tilde{\kappa}_x > \tilde{S}$, which is satisfied by all the other species, was predicted in [16] as a developmental constraint resulting from curvature driven growth of the beak. The fact that Hawaiian honeycreepers do not satisfy this constraint is related to their higher normalized tomium curvature $\tilde{\kappa}_T$ (figure 2e) and large midsagittal curvature $\tilde{\kappa}_x$ coupled with relatively low sharpening rates (figure 2d).

Looking at the normalized tomium parameters (figure 2e), we find that points lie close to the line $\tilde{\kappa}_T = 0.5 + \tilde{a}_T$. To understand what this means, we note that the depth of the tomium—the vertical distance between the tip and base denoted by D_T in figure 2b—can be calculated using equation (2.3) as $D_T \equiv -z_T(L, 0) = D_B(\tilde{\kappa}_T - \tilde{a}_T)$. Therefore, the line in figure 2e implies that $D_T/D_B \approx 0.5$ for most specimens in our dataset, with the Maui parrotbill (P. xanthophrys) and Eurasian bullfinch (P. pyrrhula) deviating from this trend due to their extreme morphology (see also figure 2f).
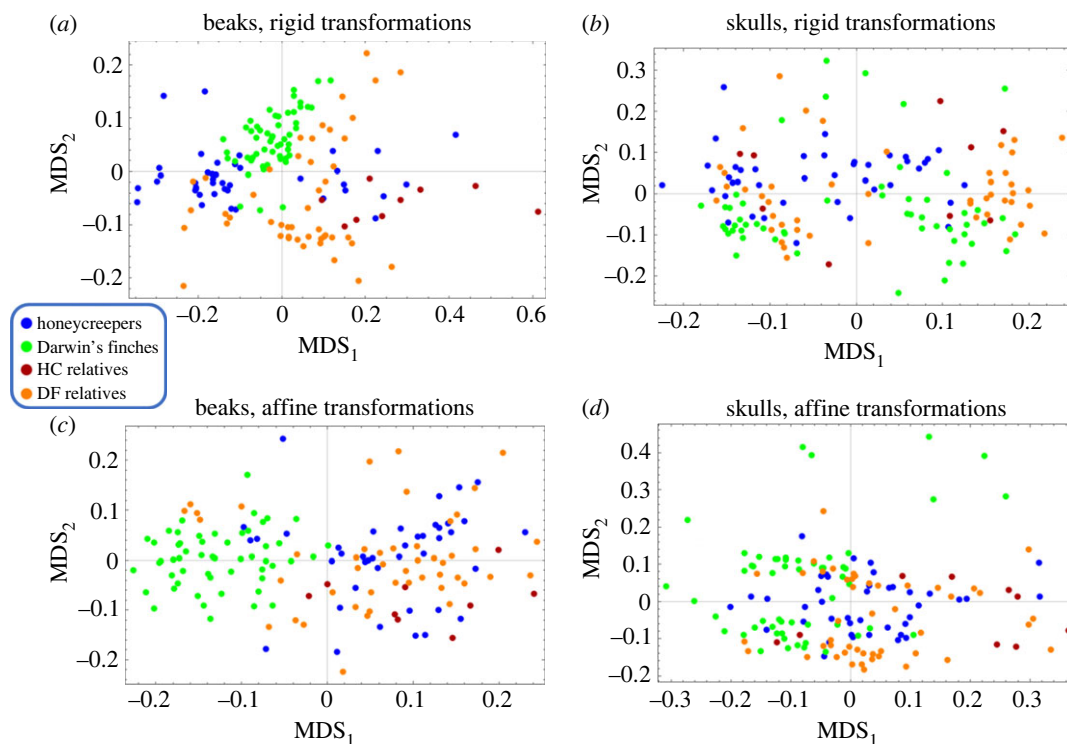
Figure 3. Multidimensional scaling (MDS) results of the surface-based morphometric analysis for the beaks and skulls. (a) Coordinates calculated using MDS analysis of the symmetric Hausdorff distance between beak meshes after optimally aligning them (with respect to the Hausdorff distance) using a rigid transformation. (b) Same as (a) but for the entire skull. (c) Same as (a) but using affine transformation for the optimal alignment. (d) Same as (a) but for entire skulls and affine transformations.

We observed that the depth over width aspect ratio D_C/W_C for the most basal cross section normal to the centreline is nearly constant for honeycreepers ($D_C/W_C = 0.64 \pm 0.1$, where 0.64 is the mean and 0.1 is the standard deviation), which is close to the value for Darwin's finches ($D_C/W_C = 0.68 \pm 0.07$), as can be seen in electronic supplementary material, figure S5B. In addition, the dimensionless curvature $\tilde{\kappa}_C$ is large for honeycreepers, especially for *V. coccinea*, as expected (figure 2f). However, this high value of dimensionless curvature is driven more by its longer length L_C than the absolute value of its curvature κ_C relative to other species (electronic supplementary material, figure S5C).

As can be seen from figures 2d–f (see also electronic supplementary material, figure S5), Honeycreepers, Darwin's finches and their respective relatives occupy distinct regions of morphospace, with Honeycreepers occupying a broader and unique range of variation in each case. This observation is also confirmed using the beak MDS coordinates from the surface-based analysis using rigid transformations (figure 3a). By contrast, the overlap between the regions occupied by the different groups in the full skull MDS plane is more significant (figure 3b). These results are consistent with the those presented in [7], in which the principal component analysis (PCA) was applied to a set of normalized landmarks representing the beaks or the full skulls. To explore further the nature of variation between the different groups, we consider MDS coordinates based on affine matching for both beaks and skulls. For beaks, we find that Darwin's finches occupy a distinct region, indicating that as a group, we cannot match their beaks with affine transformation to the other groups in our study (figure 3c).

Lastly, to quantify the relative intra-specific (within species) and interspecific (between species) variations, we compare the area of the convex hull occupied by each species (for species

that have more than two specimens) to the total area occupied by its phylogenetic group (honeycreepers or Darwin's finches). The smaller the ratio of these two areas, $\mathcal{V}$, the stronger a species' specimens are clustered together. To assess the statistical significance of the mean measured value of $\mathcal{V}$ for each phylogenetic group, we estimate its probability by randomly assigning the morphospace values (such as those given in figure 2d) to specimens and recomputing $\mathcal{V}$. We find that for the morphospaces shown in figure 2d–f and figure 3, specimens are significantly clustered (with 99% confidence) relative to other members of their respective phylogenetic group.

3. Form and feeding mechanics of beaks

Beaks are under multiple selection pressures, and their evolution may be correlated with other parts of the body due to developmental constraints or co-adaptation [24,25]. Here, we explore correlations between beak shape and diet for birds in our study [26]. We grouped species in our dataset by their main diet items following [7,27,28]. To explore the correlation between diet and the morphospace generated in the previous sections, we assign each diet category a numerical value $\mathcal{D}$, which is an integer in the range [1, 9], and then found Spearman's rank correlation coefficient—which is suitable for correlating discrete and continuous variables—between this measure and the morphometric quantity of interest (figure 4). Since the numerical value of $\mathcal{D}$ for each diet category involves an arbitrary choice of ordering the categories, we calculate the correlation coefficient for all possible permutations of assigning a value to a diet category and define the correlation coefficient as the maximum across all possible permutations. To check that this method does not
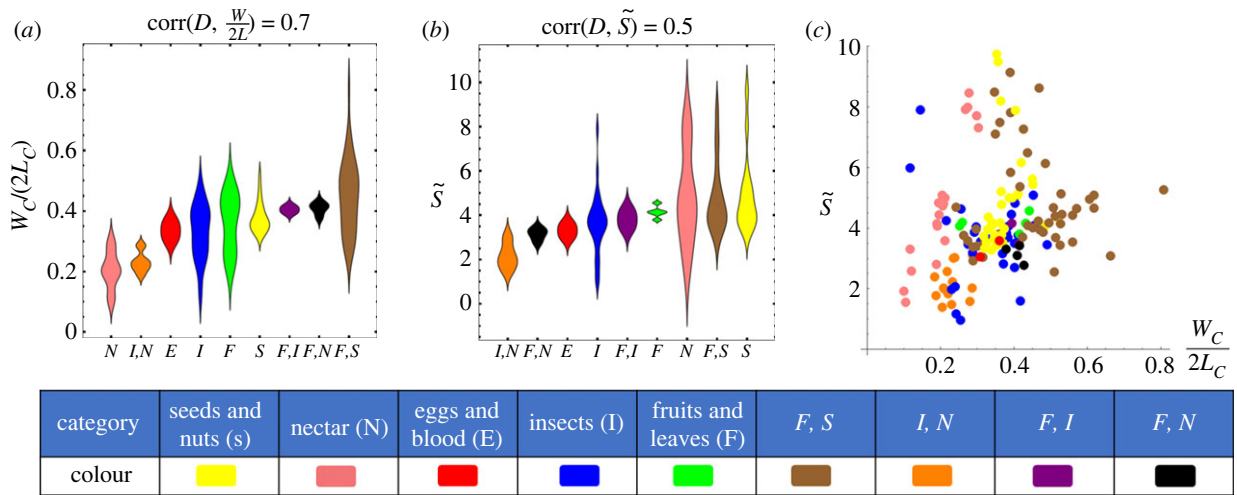
Figure 4. Diet and evolutionary morphospace. (*a*) For each diet category, we plot the aspect ratio $W_C/2L_C$ which is highly correlated with the diet value (each diet category has a value from 1 to 9 in the order shown in the figure). The correlation coefficient is $\text{Corr}[W_C/2L_C, \mathcal{D}] = 0.73$. Abbreviations: N = nectar; I = insects; S = seeds and nuts; F = fruits and leaves; E = eggs and blood. (*b*) Diet category against the sharpening rate $\tilde{S}$, with corresponding correlation coefficient $\text{Corr}[\tilde{S}, \mathcal{D}] = 0.46$. (*c*) Each specimen is represented as a point in the morphospace $(W_C/2L_C, \tilde{S})$, and colour coded according to its diet category as given in (*a*) and (*b*).

generate spurious correlations, we generate control morphospaces consisting of values chosen at random between [0,1], and then compute the correlation between these random values and $\mathcal{D}$. By repeating this for ten thousand trials, we estimate that correlations above 0.25 are statistically significant since it did not result for any of these trials.

Using this method, we find that the aspect ratio W_C/L_C is highly correlated with diet (with coefficient of 0.70), where small values correspond to nectar feeding species and large values correspond to fruit and seed eating species (figure 4*a*)—possibly enabling them to exert larger output forces on food items by increasing the mechanical advantage [29] and fracture resistance as suggested in previous studies [30–32]. We also find that fruit and seed eating species have high sharpening rate $\tilde{S}$ (coefficient ≈ 0.54, figure 4*b*), which we hypothesize enables the beak to withstand high forces, since curvature is known to enhance the rigidity of mechanical structures [33]. In addition, we find that the skull morphospace parameter MDS_2 is correlated with diet (coefficient ≈ 0.46). While these correlations may be due to morphology adapting to diet—long and narrow beaks for probing flowers, wide and deep beaks for crushing seeds, as shown in previous studies [30,34,35]—the correlation between diet and morphology may also be linked to other factors [36]. Indeed phylogenetic grouping (honeycreepers, Darwin's finches, and their respective relatives) is also highly correlated with the aspect ratio W_C/L_C (with coefficient of 0.54) and sharpening rate $\tilde{S}$ (with coefficient of 0.48).

Figure 4*c* shows the morphospace $(W_C/2L_C, \tilde{S})$ colour coded according to diet category, illustrating the correlations between these quantities and diet mentioned in the previous paragraph. By calculating the quantity $\mathcal{V}$ described at the end of §2(*b*), we find that specimens of the same species are significantly clustered in this morphospace relative to other members of their phylogenetic group.

4. Developmental biophysics of beaks

Beak growth occurs via the extrusion of a group of dividing cells near the tip of the developing beak, even as the number

of dividing cells in the growth zone diminishes over time [18]. By looking at how adult beak cross sections vary along the centreline, we find that the shape of the cross sections changes, as their size decreases towards the tip (electronic supplementary material, figure S6). This observation of three-dimensional beak shapes rules out homogeneous and isotropic contraction of the growth zone over time to explain beak shapes [18,23]. In previous work on the finch beak [16], inspired by experimental observations, we proposed a cellular model that accounts for cell proliferation patterns that vary in space–time. This led to a coarse-grained tissue-level geometric model for the evolution of the beak surface [16], given the initial size and shape of the cross section (figure 5*a*), and the extrusion rate of the growth zone along the proximal–distal axis, denoted as U. By modifying this model to account for the centreline curvature of the beaks, we show that we can generate all the beak shapes in our dataset by varying a single dimensionless parameter (describing how the dynamics of growth depends on curvature), (orange arrows in figure 5*a*).

(a) Cell-scale model for growth

In order to achieve a continuous turning of the growth zone and generate a curved beak, cells must divide and extrude faster in the upper part of the beak (culmen). A minimal model for this follows from having a linear transverse gradient in cell proliferation rates (figure 5*b*), controlled by Bmp4, known to generate the highly curved cockatiel beaks [37]. Furthermore, to account for our observation of changing shapes of cross sections, we assume that cells have a proliferation gradient along the proximal–distal axis of the beak controlled by the gradient of a morphogen that diffuses to the surrounding cells with diffusion constant D_c and degrades at a rate Γ. This limits the efficacy of the morphogen produced by a cell to a region of size $\lambda \sim \sqrt{D_c/\Gamma}$ (grey circle in figure 5*c*). Furthermore, since only cells in the growth zone produce this morphogen, a gradient along the proximal–distal axis can generate a stable protrusion rate in the distal direction.

Thus the behaviour of individual cells is a function of distance from the growth zone and the curvature of the beak. Those that are far relative to λ will receive a weaker signal
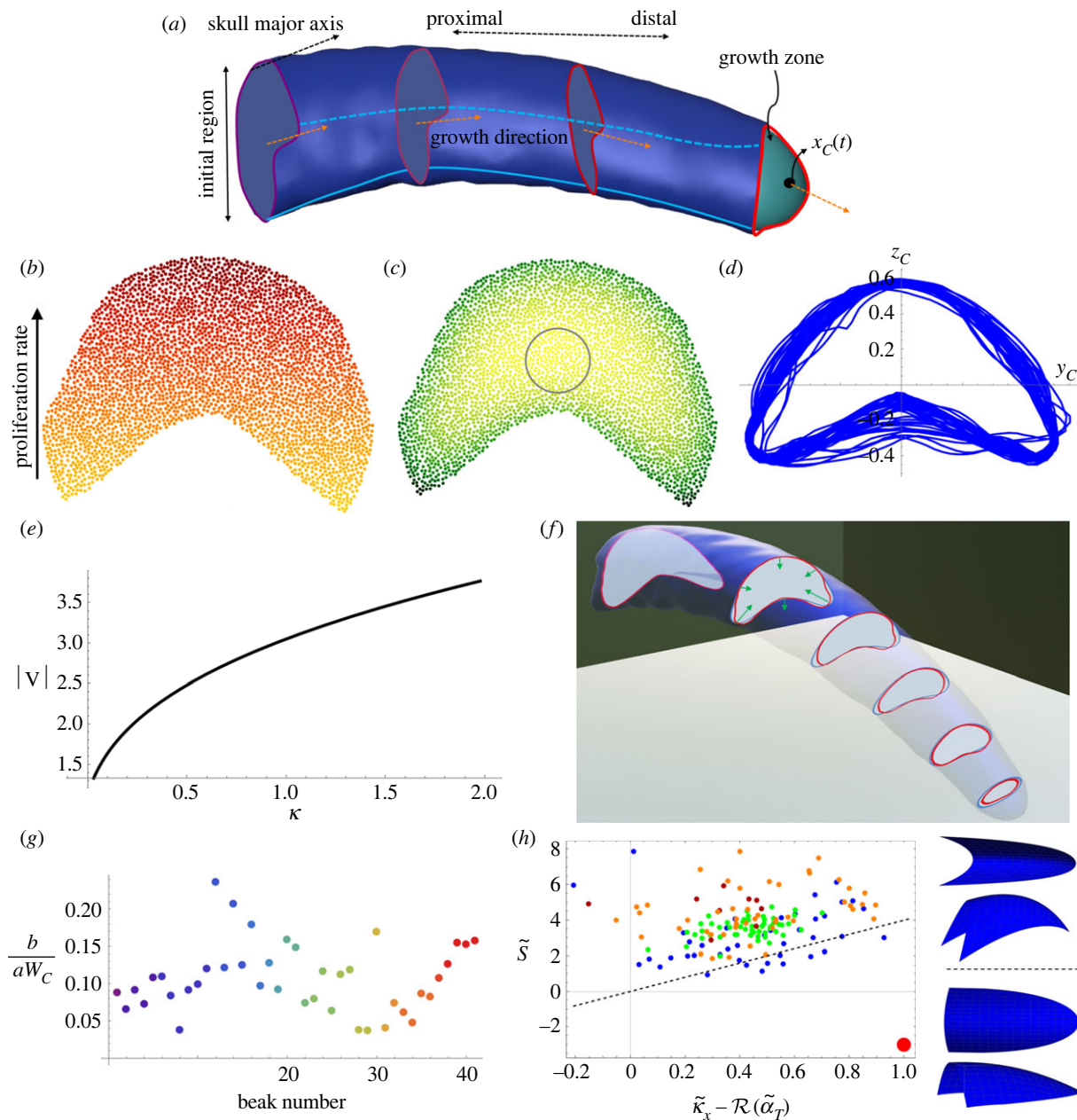
Figure 5. Beak development. (*a*) The blue mesh is taken from the *V. coccinea* sample shown in figure 2. The function $x_C(t)$ is the centre of the growth zone at time t, which is the green-blue region near the tip. Also illustrated is the direction of growth (orange arrows) and the major axis of the skull (black arrow). The red curves represent cross sections at different times, with more recent ones being brighter. (*b*) The assumed linear gradient in cell proliferation leads to a continuously turning growth direction leading to beak centreline curvature. (*c*) Morphogen concentrations from the boundary death model described in the main text, the grey circle represents the range of the morphogen. (*d*) Basal cross sections from the beaks of all honeycreeper specimens, scaled to have unit width and depth. (*e*) Speed of points on the cross section, taken at $x_C = 0.5 \, L_G$, as a function of the arc-curvature of the cross section. (*f*) Results for the same *V. coccinea* sample as in (*a*) with cross sections generated from a simulation using the mean curvature flow, $\mathbf{v} = -(a + b\kappa)\mathbf{n}$, where $\mathbf{v}$ is the velocity vector due to the evolving transverse cross sections (green arrows), κ is the arc curvature at the corresponding point on the cross section and $\mathbf{n}$ is the unit normal to the cross section at that point. The dimensionless parameter used to generate this result corresponds to $b/(aW) = 0.15$. The initial conditions were generated from a basal cross section of the actual beak. (*g*) The dimensionless parameter b/aW_C plotted for all honeycreepers, colour coded as in figure 1*c*. (*h*) The dashed line represents the constraint derived in the main text, $\tilde{\kappa}_x - \mathcal{R}(\tilde{a}_T) \leq \tilde{S}/4$, which is approximately satisfied by the honeycreeper samples in our dataset. Here $\mathcal{R}(\cdot) \equiv \max(0, \cdot)$ is the unit ramp function. The two blue meshes (each viewed from two angles) correspond to the red point, where the upper one has $\tilde{S} = -3$, $\tilde{\alpha}_T = 1$, $\tilde{\kappa}_x = 2$ and the lower one has $\tilde{S} = -3$, $\tilde{\alpha}_T = 0$, $\tilde{\kappa}_x = 1$.

than those that are closer. Similarly, cells proliferate less in more positively curved regions near the boundary (e.g. black parts in figure 5*c*). In addition to this effect, cells stop dividing at some probability P_{death}, independent of the morphogen concentration. This last effect, when acting alone, leads to an exponential decay over time of the growth zone size, without any change in its shape. Figure 5*d* shows the (scaled) basal cross sections for all honeycreeper samples,

which represent the initial conditions for the dynamical evolution discussed in the next section.

(b) Tissue-scale model for growth

We now consider a tissue level continuum approximation of the cellular model described above. Since cells near a curved part of the growth zone boundary receive the morphogen

signal from fewer neighbours (figure 5c), the envelope of the growth zone will shrink faster in those regions. By looking at transverse sections of the adult beaks, represented using equation (2.1), we observe that regions of higher curvature (near $y = 0$) do in fact shrink faster (figure 5e). Therefore, this suggests that the boundary of the growth zone evolves with a velocity that depends on the local (arc) curvature through the relation, first introduced by us in this context to explain the shapes of finch beaks [16],

$$\mathbf{v} \equiv \partial_t \mathbf{x} = -(a + b\kappa)\mathbf{n}, \quad a, b > 0, \tag{4.1}$$

where $\mathbf{n}$ is the inward normal to the surface, and κ is the planar curvature of the boundary. The characteristic length scale given by the ratio b/a determines which of the two terms in the growth law will dominate. When $\kappa^{-1} \gg b/a$, the velocity of the front is a constant and follows Huygens' principle. When $\kappa^{-1} \ll b/a$, the front velocity $\mathbf{v} \sim -b\kappa\mathbf{n}$, and corresponds to the well-known curve shortening (or mean curvature) flow in which speed is proportional to the curvature [38,39].

Figure 5f shows the agreement between the shape generated by the mean curvature flow and the cross sections of a *V. coccinea* sample (see also electronic supplementary material, figure S7). By fitting the mean curvature flow to beak cross sections, we obtain the dimensionless parameter $b/(aW_C)$, which is plotted in figure 5g.

(c) Developmental constraints in morphospace

Our generative model which was inspired by the developmental biology of the beak can not only reproduce beak shapes, but also provides limits on the range of allowable beak shapes. For example, beak shapes generated by equation (4.1), when a and b are both positive, will have cross-sectional area and perimeter that decrease over time (electronic supplementary material, figure S6A–B) so that their cross sections become more convex and circular as we approach the tip (electronic supplementary material, figure S6C–D).

To investigate the constraints on beak shape that follow from the curvature-driven flow described in equation (4.1), we simplify equation (4.1) by assuming circular cross sections with radius $R(t) = W(t)/2$, where $W(t)$ is the width of the beak as a function of time, which we will calculate using the tomium width given in equation (2.4). Then $\kappa(t) = 1/R(t) = 2/W(t)$ and plugging this into equation (4.1), we obtain

$$\frac{\mathrm{d}R(t)}{\mathrm{d}t} = -\left(a + \frac{b}{R}\right). \tag{4.2}$$

To convert between spatial (x_C) and temporal variables (t), we use the extrusion speed U so that $(t - t^*)U = x_C$, where $t^* = L_C/U$ is the final time when the cross section shrinks to zero size at the tip of the developed beak. Near the tip ($x_C \to 0$), the term proportional to b in equation (4.2) dominates and we get

$$W = 2R = 2\sqrt{2b(t^* - t)} = 2\sqrt{\frac{2bx_C}{U}}, \quad (x_C \to 0). \tag{4.3}$$

In §2(a), we found that the beak width is given by equation (2.4), which—using equation (2.2) and the relations $\tilde{\kappa}_{\mathrm{tip}} = 4 + \tilde{S}$ and $\tilde{a}_U = 1 + \tilde{\kappa}_x$ derived in §2(b)—leads to the following when ($x \to 0$),

$$W(x) = W_B \sqrt{\frac{4(1 + \tilde{\kappa}_x - \tilde{a}_T)}{4 + \tilde{S}}} \sqrt{\frac{x}{L_B}}, \quad (x \to 0). \tag{4.4}$$

After using the Pythagorean theorem to estimate the factor $x_C/x = \sqrt{1 + \alpha_T^2}$ near the tip and equating the right-hand sides of equations (4.3)–(4.4), we get

$$\frac{b}{UW_B} = \frac{(1 + \tilde{\kappa}_x - \tilde{a}_T)}{4 + \tilde{S}} \frac{L_C}{L_B\sqrt{1 + a_T^2}} \frac{W_B}{2L_C}, \tag{4.5}$$

Since the beak shrinks to a point at the tip, we require that $a > 0$, $b > 0$. Therefore, for a given value of b, the largest possible beak length L_C corresponds to the case $a = 0$ (since a higher value of a reduces the length via faster shrinking of the growth zone). Then, from equation (4.2), it follows that $\dot{R} = -b/R$ so that $R(t) = \sqrt{2b(L_C/U - t)}$. Given the initial conditions $R(0) = W_B/2 = \sqrt{2bL_C/U}$, this means that $b/U = W_B^2/8L_C$. Since larger values of the beak length require negative values of a, we get the prediction $b/(W_B U) < W_B/8L_C$, which can be rewritten using equation (4.5) to eliminate b in terms of other morphological parameters and gives

$$4(1 + \tilde{\kappa}_x - \tilde{a}_T) \le \frac{L_B}{L_C}\sqrt{1 + a_T^2}(4 + \tilde{S}). \tag{4.6}$$

Empirically, we find that the factor multiplying $(4 + \tilde{S})$ is very close to unity, which follows geometrically from the fact that beak centrelines are not extremely curved, a_T, $\tilde{\kappa}_C \lesssim 1$. Therefore, we may simplify the constraint to $4(\tilde{\kappa}_x - \tilde{a}_T) \le \tilde{S}$, which reduces to the earlier result [16] $4\tilde{\kappa}_x \le \tilde{S}$ when $\tilde{a}_T = 0$. Since all other species satisfy the constraint $4\tilde{\kappa}_x \le \tilde{S}$ and have $a_T \le 0$ unlike honeycreepers (figure 2; electronic supplementary material, figure S3B), we introduce the ramp function $\mathcal{R}(\cdot) \equiv \max(0, \cdot)$ and write the constraint as $4(\tilde{\kappa}_x - \mathcal{R}(\tilde{a}_T)) \le \tilde{S}$. Figure 5h shows that honeycreeper beaks are closer to the boundary predicted by this constraint, which may be compared with two examples of beak shapes that would not be possible due to this constraint (blue meshes in figure 5h).

5. Conclusion

This study continues our previous study [16] by developing and deploying three-dimensional morphometric approaches to quantify three-dimensional beak shape and link evolution and development, now going beyond finch beaks to other avian radiations. Our methods complement (semi)landmark-based morphometrics by fully describing beak shape using a small set of geometrically meaningful parameters—orientation relative to the skull, aspect ratios and curvatures—that allow us to discover further regularities in beak shape (e.g. figure 2e; electronic supplementary material, figure S5A). This sets the stage for computational studies that can simulate the performance of different beak shapes (e.g. its mechanical rigidity) as the morphological parameters are varied to shed light on the distribution of species in morphospace [16,32,35]. The quantitative compression inherent in the mathematical form of beaks allowed us to adapt our previous biophysical model [16] to characterize curvature-dependent beak development driven by morphogen signalling. Additionally, we were able to predict developmental constraints—regions in morphospace that cannot be generated through that developmental programme—further elucidating patterns of beak shape variation in morphospace. Finally, our approach of extracting the beak centreline and transverse cross sections, and analysing their shapes as a function of distance from the tip may prove

useful for elucidating morphology and development of other tip growing systems, such as deer antlers.

Our analysis uncovered interesting patterns in morphospace, including that HC beaks occupy a broader region of morphospace, a finding we validated through employing parameter-free, mesh-based methods using the Hausdorff distance and MDS (figure 3). The mesh-based comparative analysis also showed that DF beaks occupy a distinct region of morphospace (figure 3a), even with affine transformations that lead to overlap in regions occupied by other taxa (figure 3c). Surprisingly, we found that some highly curved beaks, such as those of *V. coccinea*, do not have a high value of centreline curvature in absolute units, but rather have a high value of the (scale invariant) quantity curvature times length ($\tilde{\kappa}_C$). We also explored the relation between beak shape and diet and find a correlation that we can rationalize by considering the beak as a mechanical tool for feeding [34,40,41]. In particular, the width-to-length aspect ratio and the sharpening rate (how fast the curvature of transverse sections increases towards the tip) are highly correlated with diet.

To further understand the source of variation in HC beak morphology, we employed developmental models that use adult beak shape to glean information about beak ontogeny. While assuming a single growth direction, parallel to the major axis of the beak, was sufficient to generate DF beaks [16], generating HC beaks required a changing growth direction by assuming a linear gradient in cell proliferation rates (figure 5). With this modification, our developmental model explains how beak shape emerges due to initial size, shape, growth direction relative to the skull, the extrusion velocity of the growth zone, and the transverse shrinkage rate determined by both a and b parameters. Remarkably, a single dimensionless parameter, $b/(aW_C)$, determined how cross sectional shape evolves along the centreline for all species in our dataset.

The fact that honeycreepers occupy a broader range of morphospace in our analysis, and required a modification of our developmental model to account for centreline curvature, raises the question of how this group managed to escape the constraint that limited the variation of other birds in our dataset. Applying the methods developed in this paper in conjunction with experimental work on developing beaks to a wider range of avian taxa would be natural next steps towards a more comprehensive description of beak shaping during development, its evolution across time, and its function as a remarkably adaptable tool.

References

1. Lerner HRL, Meyer M, James HF, Hofreiter M, Fleischer RC. 2011 Multilocus resolution of phylogeny and timescale in the extant adaptive radiation of Hawaiian honeycreepers. *Curr. Biol.* **21**, 1838–1844. (doi:10.1016/j.cub.2011.09.039)

2. Clements JF, Schulenberg TS, Iliff MJ, Fredericks TA, Gerbracht JA, Lepage D, Billerman SM, Sullivan BL, Wood CL. 2022 The eBird/Clements checklist of Birds of the World: v2022. Downloaded from https://www.birds.cornell.edu/clementschecklist/download/.

3. Bookstein FL. 1996 Combining the tools of geometric morphometrics. In *Advances in morphometrics*, pp. 131–151. New York, NY: Springer.

4. Adams DC, Rohlf FJ, Slice DE. 2004 Geometric morphometrics: ten years of progress following the 'revolution'. *Ital. J. Zool.* **71**, 5–16. (doi:10.1080/11250000409356545)

5. Grant BR, Grant PR. 1993 Evolution of Darwin's finches caused by a rare climatic event. *Proc. R. Soc. Lond. B* **251**, 111–117. (doi:10.1098/rspb.1993.0016)

6. Foster DJ, Podos J, Hendry AP. 2008 A geometric morphometric appraisal of beak shape in Darwin's finches. *J. Evol. Biol.* **21**, 263–275. (doi:10.1111/j.1420-9101.2007.01449.x)

7. Tokita M, Yano W, James HF, Abzhanov A. 2017 Cranial shape evolution in adaptive radiations of birds: comparative morphometrics of Darwin's finches and Hawaiian honeycreepers. *Phil. Trans. R. Soc. B* **372**, 20150481. (doi:10.1098/rstb.2015.0481)

8. Gunz P, Mitteroecker P. 2013 Semilandmarks: a method for quantifying curves and surfaces. *Hystrix Ital. J. Mammal.* **24**, 103–109.

9. Bardua C, Felice RN, Watanabe A, Fabre AC, Goswami A. 2019 A practical guide to sliding and surface semilandmarks in morphometric analyses. *Integr. Organismal Biol.* **1**, obz016. (doi:10.1093/iob/obz016)

10. Palci A, Lee MS. 2019 Geometric morphometrics, homology and cladistics: review and recommendations. *Cladistics* **35**, 230–242. (doi:10.1111/cla.12340)

11. Toussaint N et al. 2021 A landmark-free morphometrics pipeline for high-resolution phenotyping: application to a mouse model of Down syndrome. *Development* **148**, dev188631. (doi:10.1242/dev.188631)

12. Harper CM, Goldstein DM, Sylvester AD. 2022 Comparing and combining sliding semilandmarks and weighted spherical harmonics for shape analysis. *J. Anat.* **240**, 678–687. (doi:10.1111/joa.13589)

13. Raup DM, Michelson A. 1965 Theoretical morphology of the coiled shell. *Science* **147**, 1294–1295. (doi:10.1126/science.147.3663.1294)

14. Raup DM. 1966 Geometric analysis of shell coiling: general problems. *J. Paleontol.* **40**, 1178–1190.

15. Contreras-Figueroa G, Aragón JL. 2023 A mathematical model for mollusc shells based on parametric surfaces and the construction of theoretical morphospaces. *Diversity* **15**, 431. (doi:10.3390/d15030431)

16. Al-Mosleh S, Choi GPT, Abzhanov A, Mahadevan L. 2021 Geometry and dynamics link form, function, and evolution of finch beaks. *Proc. Natl Acad.*

Sci. **118**, e2105957118. (doi:10.1073/pnas.2105957118)

17. Abzhanov A, Protas M, Grant BR, Grant PR, Tabin CJ. 2004 Bmp4 and morphological variation of beaks in Darwin's finches. *Science* **305**, 1462–1465. (doi:10.1126/science.1098095)

18. Fritz JA, Brancale J, Tokita M, Burns KJ, Hawkins MB, Abzhanov A, Brenner MP. 2014 Shared developmental programme strongly constrains beak shape diversity in songbirds. *Nat. Commun.* **5**, 1–9. (doi:10.1038/ncomms4700)

19. Huttenlocher DP, Klanderman GA, Rucklidge WJ. 1993 Comparing images using the Hausdorff distance. *IEEE Trans. Pattern Anal. Mach. Intell.* **15**, 850–863. (doi:10.1109/34.232073)

20. Dubuisson MP, Jain AK. 1994 A modified Hausdorff distance for object matching. In *Proc. of 12th Int. Conf. on Pattern Recognition*, vol. 1, pp. 566–568. Piscataway, NJ: IEEE.

21. Torgerson WS. 1952 Multidimensional scaling: I. Theory and method. *Psychometrika* **17**, 401–419. (doi:10.1007/BF02288916)

22. Cox MAA, Cox TF. 2008 Multidimensional scaling. In *Handbook of data visualization* (eds C Chen, W Härdle, A Unwin), pp. 315–347. New York, NY: Springer.

23. Campàs O, Mallarino R, Herrel A, Abzhanov A, Brenner MP. 2010 Scaling and shear transformations capture beak shape variation in Darwin's finches. *Proc. Natl Acad. Sci. USA* **107**, 3356–3360. (doi:10.1073/pnas.0911575107)

24. Navalón G, Marugán-Lobón J, Bright JA, Cooney CR, Rayfield EJ. 2020 The consequences of craniofacial integration for the adaptive radiations of Darwin's finches and Hawaiian honeycreepers. *Nat. Ecol. Evol.* **4**, 270–278. (doi:10.1038/s41559-019-1092-y)

25. Navalón G, Bright JA, Marugán-Lobón J, Rayfield EJ. 2019 The evolutionary relationship among beak shape, mechanical advantage, and feeding ecology in modern birds. *Evolution* **73**, 422–435. (doi:10.1111/evo.13655)

26. Pigot AL *et al.* 2020 Macroevolutionary convergence connects morphological form to ecological function in birds. *Nat. Ecol. Evol.* **4**, 230–239. (doi:10.1038/s41559-019-1070-4)

27. Pratt HD 2005 *The Hawaiian honeycreepers: Drepanidinae*. Oxford, UK: Oxford University Press.

28. del Hoyo J, Elliott A, Sargatal J, Christie D, De Juana E. 2018 *Handbook of the birds of the world alive*. Barcelona, Spain: Lynx Edicions, 2014.

29. Uicker JJ, Pennock GR, Shigley JE, Mccarthy JM 2003 *Theory of machines and mechanisms*, vol. 3. New York, NY: Oxford University Press.

30. Boag PT, Grant PR. 1981 Intense natural selection in a population of Darwin's finches (Geospizinae) in the Galapagos. *Science* **214**, 82–85. (doi:10.1126/science.214.4516.82)

31. Witmer LM, Rose KD. 1991 Biomechanics of the jaw apparatus of the gigantic Eocene bird Diatryma: implications for diet and mode of life. *Paleobiology* **17**, 95–120. (doi:10.1017/S0094837300010435)

32. Soons J *et al.* 2010 Mechanical stress, fracture risk and beak evolution in Darwin's ground finches (Geospiza). *Phil. Trans. R. Soc. B* **365**, 1093–1098. (doi:10.1098/rstb.2009.0280)

33. Lazarus A, Florijn H, Reis PM. 2012 Geometry-induced rigidity in nonspherical pressurized elastic shells. *Phys. Rev. Lett.* **109**, 144301. (doi:10.1103/PhysRevLett.109.144301)

34. Soons J, Herrel A, Genbrugge A, Aerts P, Podos J, Adriaens D, de Witte Y, Jacobs P, Dirckx J. 2010 Mechanical stress, fracture risk and beak evolution in Darwin's ground finches (Geospiza). *Phil. Trans. R. Soc. B* **365**, 1093–1098. (doi:10.1098/rstb.2009.0280)

35. Soons J, Genbrugge A, Podos J, Adriaens D, Aerts P, Dirckx J, Herrel A. 2015 Is beak morphology in Darwin's finches tuned to loading demands? *PLoS ONE* **10**, e0129479. (doi:10.1371/journal.pone.0129479)

36. Bright JA, Marugán-Lobón J, Cobb SN, Rayfield EJ. 2016 The shapes of bird beaks are highly controlled by nondietary factors. *Proc. Natl Acad. Sci. USA* **113**, 5352–5357. (doi:10.1073/pnas.1602683113)

37. Wu P, Jiang TX, Shen JY, Widelitz RB, Chuong CM. 2006 Morphoregulation of avian beaks: comparative mapping of growth zone activities and morphological evolution. *Dev. Dyn.* **235**, 1400–1412. (doi:10.1002/dvdy.20825)

38. Rayleigh L. 1942 The ultimate shape of pebbles, natural and artificial. *Proc. R. Soc. Lond. A* 107–118. (doi:10.1098/rspa.1942.0065)

39. Mullins WW. 1956 Two-dimensional motion of idealized grain boundaries. *J. Appl. Phys.* **27**, 900–904. (doi:10.1063/1.1722511)

40. Grant PR. 1981 The feeding of Darwin's finches on *Tribulus cistoides* (L.) seeds. *Anim. Behav.* **29**, 785–793. (doi:10.1016/S0003-3472(81)80012-7)

41. Herrel A, Soons J, Aerts P, Dirckx J, Boone M, Jacobs P, Adriaens D, Podos J. 2010 Adaptation and function of the bills of Darwin's finches: divergence by feeding type and sex. *Emu* **110**, 39–47. (doi:10.1071/MU09034)

42. Mosleh S, Choi GPT, Musser GM, James HF, Abzhanov A, Mahadevan L. 2023 Data from: Beak morphometry and morphogenesis across avian radiations. Harvard Dataverse. (doi:10.7910/DVN/UQQ6EZ)

43. Mosleh S, Choi GPT, Musser GM, James HF, Abzhanov A, Mahadevan L. 2023 Beak morphometry and morphogenesis across avian radiations. Figshare. (doi:10.6084/m9.figshare.c.6806634)